

## Kinetic theory of collisionless tearing at the magnetopause

William Daughton<sup>1</sup>

Department of Physics and Astronomy, University of Iowa, Iowa City, Iowa, USA

H. Karimabadi

Department of Electrical and Computer Engineering, University of California, San Diego, La Jolla, California, USA

Received 16 August 2004; revised 21 December 2004; accepted 7 January 2005; published 22 March 2005.

[1] This paper is the first in a series of three with the aim of addressing one of the controversial issues at the magnetopause, namely the location where reconnection first occurs during periods of a large interplanetary magnetic field  $B_y$ . In this first paper, the linear properties of the collisionless tearing mode are reexamined as a function of the guide field  $B_y$  using a formally exact approach for computing the nonlocal Vlasov stability of a current layer. Three distinct parameter regimes are identified depending on the degree to which electron orbits are modified by the guide field in the central region of the current layer. In the limit of both weak and strong guide field, the fastest-growing tearing mode has a wave vector  $k_x$  perpendicular to the direction of the current, in agreement with previous theoretical treatments. However, for intermediate values of the guide field where the electrons begin to transition to magnetized orbits, the fastest-growing modes have a finite wave vector  $k_y$  in the direction of the current. In this newly discovered regime, the so-called drift tearing modes have finite real frequency and propagate in the direction of the electron diamagnetic drift with growth rates 10–50% larger than the conventional tearing instability. Maximum growth occurs for a propagation angle in the range  $\theta = \tan^{-1}(k_y/k_x) \approx 6\text{--}10^\circ$ . These new predictions are confirmed using fully kinetic particle-in-cell simulations. The structure of the out-of-plane magnetic field perturbation predicted by nonlocal Vlasov theory is examined as a function of guide field. In the limit of a neutral sheet, the quadrupole structure has a characteristic scale near the electron meandering width and shows significant differences with the predictions of linear Hall MHD. The addition of a guide field strongly distorts the quadrupole structure and compresses the spatial extent. In the strong guide field limit, the width of the out-of-plane magnetic field perturbation is reduced to the electron gyroscale in the guide field. During the onset phase, these structures represent a distinct signature of the collisionless tearing mode that is significantly different than the typical ion-scale quadrupole pattern from fast reconnection. Finally, we note that the tearing mode maintains a significant growth rate over a large range of guide field so that component merging cannot be ruled out based on linear theory.

**Citation:** Daughton, W., and H. Karimabadi (2005), Kinetic theory of collisionless tearing at the magnetopause, *J. Geophys. Res.*, 110, A03217, doi:10.1029/2004JA010751.

### 1. Introduction

[2] Magnetic reconnection is now recognized as the dominant transport mechanism at the magnetopause during periods of southward IMF [Baumjohann and Paschmann, 1987]. However, there exist important gaps in our understanding of the details of how and where reconnection

occurs. One of the critical issues is to identify where the reconnection line on the dayside magnetopause is formed during periods of a large interplanetary magnetic field  $B_y$  (the so-called guide field). Two competing models have been proposed. The antiparallel merging model [Crooker, 1979; Luhmann *et al.*, 1984] predicts that reconnection would occur where the magnetic shear across the magnetopause is largest and predicts no reconnection in the subsolar region when the IMF  $B_y$  is large. This is to be contrasted with the component merging model [Sonnerup, 1974; Gonzalez and Mozer, 1974], which predicts that the reconnection line passes through the subsolar point and has an orientation that is controlled by the IMF. Observations of

<sup>1</sup>Also at Los Alamos National Laboratory, Los Alamos, New Mexico, USA.

the magnetopause have yielded contradictory interpretations. For instance, *Gosling et al.* [1990] used observations of events at low latitude and in one case for a magnetic shear as small as  $60^\circ$  to argue against antiparallel merging and in favor of component merging. More recent evidence in favor of component merging has also been reported [*Kim et al.*, 2002; *Moore et al.*, 2002; *Sonnerup et al.*, 2004]. These studies are to be contrasted with those of *Newell et al.* [1995, and references therein], which concluded that local magnetic shear and not location is most important in determining whether merging occurs.

[3] Although theoretical studies of reconnection at the magnetopause have focused on the collisionless tearing mode [*Coppi et al.*, 1966; *Laval et al.*, 1966; *Biskamp and Schindler*, 1971; *Sonnerup*, 1974] as the onset mechanism, the results have been inconclusive. The linear properties of the tearing mode for neutral sheet geometry and with the addition of a guide field have been considered by numerous authors [*Drake and Lee*, 1977; *Galeev and Zelenyi*, 1978; *Quest and Coroniti*, 1981a, 1981b; *Gladd*, 1990; *Ding et al.*, 1992]. In particular, *Quest and Coroniti* [1981b] compared the growth rate to the magnetosheath flow time from the nose of the magnetopause to the equatorward edge of the polar cusp. This provides a measure of the tearing efficiency as for longer times the wave will be convected to the nightside before growing appreciably. They concluded that only thin magnetopause current sheets can satisfy the criterion that the tearing growth time is much less than the flow time. Furthermore, they showed that the presence of a guide field can reduce the growth rate by as much as an order of magnitude or more. Considering thicker sheets, *Gladd* [1990] concluded that the tearing mode growth rate is too small by 1–2 orders of magnitude and reiterated *Galeev et al.*'s [1986] suggestion that other mechanisms such as anomalous resistivity may be required to obtain substantially larger growth rates. *Chen and Palmadesso* [1984] showed that an ion temperature anisotropy, which is often observed in the magnetosheath, could also enhance the tearing mode growth rate and that for relatively thick current layers the ion anisotropy can increase the growth rate by 1–2 orders of magnitude [*Burkhart and Chen*, 1989].

[4] The nonlinear evolution of the collisionless tearing mode is less well understood than the linear theory. Early theoretical studies ruled out component-merging as a possibility. Nonlinear theories of the tearing mode in the presence of a guide field [*Drake and Lee*, 1977; *Coroniti and Quest*, 1984] showed that the tearing mode saturates at minute amplitudes (50 m), much smaller than the magnetopause current layer thickness of 50–200 km. We refer the reader to *Karimabadi et al.* [2005a, hereinafter referred to as Paper II] for a review of these theories.

[5] The above studies have been hampered by several factors. Analytical calculations of the tearing mode are notoriously difficult due to the complex particle orbits, and the approximations break down in the limit of thin current sheets often observed at the magnetopause. Particle simulations of the tearing mode, which are used to study the nonlinear evolution and saturation amplitude, are also very difficult to perform. These simulations need to be performed with high resolution and in a regime where the singular layer thickness is well separated from other scales

in the problem (e.g., the sheet thickness, debye length, ion gyroradius, etc.). As it turns out, these requirements are computationally challenging and even the more recent studies of guide field tearing have bypassed the issue of nonlinear saturation by imposing an initial, large perturbation in the problem to avoid the onset phase and proceed to fully developed fast reconnection [*Hesse et al.*, 2002].

[6] Recognizing the above limitations, we have taken a new approach. In this series of three papers, the linear and nonlinear evolution of the tearing instability is examined for a range of guide fields relevant to the magnetopause. In the first paper, a novel approach for computing the Vlasov stability of thin current sheets is used to reexamine the linear properties of the tearing mode as a function of the guide field. This approach allows one to compute formally exact eigenmodes of the Vlasov-Maxwell system with approximations arising only in the discretization of the equations. Our second paper [*Karimabadi et al.*, 2005a, hereinafter referred to as Paper II] deals with the nonlinear evolution and saturation mechanism of a single tearing mode, while the third paper [*Karimabadi et al.*, 2005b, hereinafter referred to as Paper III] deals with the nonlinear evolution in the presence of multiple modes with a detailed discussion of the results in terms of reconnection onset at the magnetopause.

[7] The main new results in this manuscript are (1) the identification of a new regime of collisionless tearing with properties intermediate between the zero and strong guide field limits. In this new regime, the fastest-growing modes have a finite wave vector  $k_y$  in the direction of the current. This unexpected result is verified using fully kinetic simulation to examine the evolution of the tearing mode in the linear regime. These so-called drift tearing modes propagate in the direction of the electron diamagnetic drift with growth rates 10–50% larger than the conventional tearing instability. Maximum growth occurs for a propagation angle in the range  $\theta = \tan^{-1}(k_y/k_x) \approx 6\text{--}10^\circ$ , giving rise to a complex resonance structure in three dimensions. (2) The nonlocal linear Vlasov approach is used to compute the out-of-plane magnetic field perturbation in the linear regime. In the zero guide field limit the perturbation has a quadrupole structure, but with the introduction of a guide field the pattern is highly distorted and the spatial scale is reduced to the electron gyroscale. (3) The linear growth rate remains competitive to the antiparallel case even for relatively large values of the guide field. The relevance of this finding in regard to viability of component merging will be explored in more detail in Paper II.

[8] The manuscript is organized as follows. Section 2 describes the equilibrium used in this study, while section 3 describes the linear Vlasov code that is used for all nonlocal linear calculations. The results are presented in section 4, and the conclusions are summarized in section 5.

## 2. Equilibrium

[9] The *Harris* [1962] equilibrium is considered with the addition of a uniform guide field

$$\begin{aligned} B_y &= B_{y0}, \\ B_x &= B_{x0} \tanh\left(\frac{z}{L}\right), \end{aligned} \quad (1)$$

where  $L$  is the half thickness of the current sheet. The magnetic field component  $B_x(z)$  is produced self-consistently by the current within the sheet

$$J_y = \frac{cB_{x0}}{4\pi L} \operatorname{sech}^2\left(\frac{z}{L}\right),$$

while the  $B_y$  component of the magnetic field is externally applied.

[10] The equilibrium distributions are

$$f_s = \frac{n(z)}{\pi^{3/2} v_{th_s}^3} \exp\left[-\frac{v_x^2 + (v_y - U_s)^2 + v_z^2}{v_{th_s}^2}\right], \quad (2)$$

where  $s = i, e$  for ions and electrons,  $v_{th_s} \equiv (2T_s/m_s)^{1/2}$  is the thermal velocity,  $U_s$  is the fluid velocity in the  $y$ -direction,  $T_s$  is the temperature,  $m_s$  is the mass, and the density profile is

$$n(z) \equiv n_o \operatorname{sech}^2\left(\frac{z}{L}\right). \quad (3)$$

The equilibrium force balance imposes the constraint

$$n_o(T_e + T_i) = \frac{B_{x0}^2}{8\pi}, \quad (4)$$

and to enforce charge neutrality, one must require  $U_i/T_i = -U_e/T_e$ . The drift velocities are chosen to be the diamagnetic drifts resulting from the two-fluid description

$$U_s = \frac{2cT_s}{q_s B_o L}. \quad (5)$$

[11] In this manuscript the parameters characterizing the equilibrium are given in terms of dimensionless parameters. The Harris equilibrium with a guide field is characterized by the five dimensionless parameters

$$\frac{\rho_i}{L}, \quad \frac{m_i}{m_e}, \quad \frac{T_i}{T_e}, \quad \frac{B_{y0}}{B_{x0}}, \quad \frac{\omega_{pe}}{\Omega_{ce}},$$

where  $\rho_i = v_{th_i}/\Omega_{ci}$  is an ion gyroradius,  $v_{th_i} = (2T_i/m_i)^{1/2}$  is the ion thermal speed,  $\Omega_{cs} = eB_{x0}/(m_s c)$  is the gyrofrequency computed from the asymptotic field  $B_{x0}$ , and  $\omega_{pe} = (4\pi n_o e^2/m_e)^{1/2}$  is the electron plasma frequency calculated from the central density  $n_o$ . The ratio of the ion fluid to thermal velocity may be expressed as  $U_i/v_{th_i} = \rho_i/L$  and the constraint (4) permits the electron thermal velocity to be written as  $v_{th_e}/c = [\sqrt{1 + T_i/T_e}(\omega_{pe}/\Omega_{ce})]^{-1}$ . A comprehensive study examining variations in all of these equilibrium parameters is beyond the scope of the present manuscript and furthermore is largely unnecessary since many of the basic dependencies are well known. Instead, the focus is directed toward the basic properties of the tearing mode as a function of the guide field  $B_{y0}/B_{x0}$ . For this

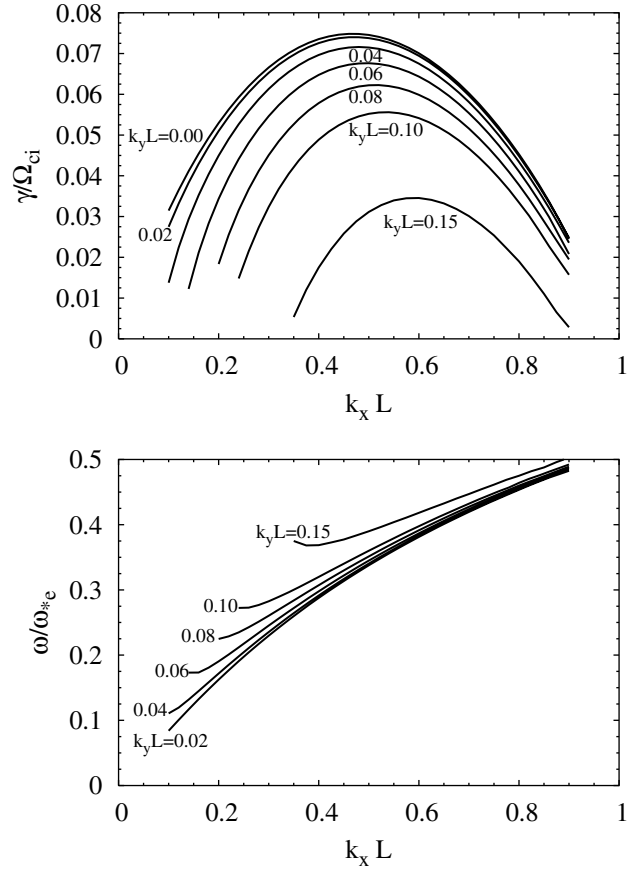


**Figure 1.** Dispersion relation in the limit of no guide field  $B_{y0} = 0$ . The (top) growth rate normalized to  $\Omega_{ci}$  and (bottom) real frequency normalized to  $\omega_{*e} \equiv k_y U_e$  are given as a function of  $k_x$  and  $k_y$  for the equilibrium parameters in (6).

purpose, four of the dimensionless equilibrium parameters are held fixed for most of the results presented

$$\frac{\rho_i}{L} = 1, \quad \frac{m_i}{m_e} = 1836, \quad \frac{T_i}{T_e} = 1, \quad \frac{\omega_{pe}}{\Omega_{ce}} = 5, \quad (6)$$

which implies  $v_{th_e}/c \approx 0.14$  is also held fixed.

### 3. Linear Vlasov Theory

[12] The linear properties of the tearing mode are calculated using the formally exact approach described in the work of *Daughton* [1999]. This method employs a normal mode stability calculation using a full Vlasov description for both ions and electrons. The orbit integrals arising from the linear Vlasov theory are treated numerically using the exact unperturbed particle orbits and including the form of the perturbation inside the integral. Both electromagnetic and electrostatic contributions to the field perturbation are retained and resulting system of integro-differential equations is solved using a basis function expansion of the eigenfunction. As discussed by *Daughton* [2003], the addition of a guide field introduces a few important complications, but the method remains formally exact. The results

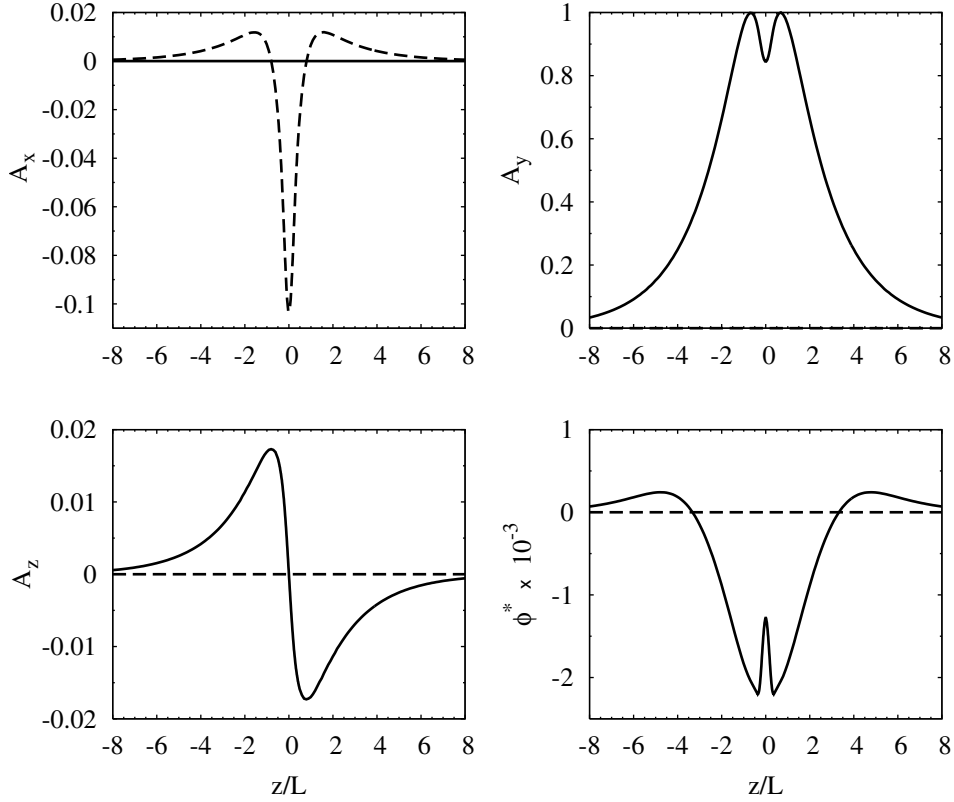


**Figure 2.** Example eigenfunction for a tearing mode in the limit of no guide field  $B_{y0} = 0$  with equilibrium parameters in (6). The solid and dashed lines denote the real and imaginary parts of  $A_x$ ,  $A_y$ ,  $A_z$  and  $\phi^* \equiv \phi(\omega_{pe}/\Omega_{ce})$ . The wave vector is  $k_x L = 0.50$ ,  $k_y L = 0$  and the growth rate is  $\gamma/\Omega_{ce} = 0.075$ .

presented in this manuscript were calculated using the linear Vlasov code described by *Daughton* [2003] and we refer interested readers to this reference for a detailed description. The basic strategy involves a normal mode calculation for perturbations of the form

$$\hat{\phi} = \tilde{\phi}(z) \exp(-i\omega t + ik_y y + ik_x x), \quad (7)$$

$$\hat{\mathbf{A}} = \tilde{\mathbf{A}}(z) \exp(-i\omega t + ik_y y + ik_x x),$$

where the complex functions  $\hat{\phi}$ ,  $\hat{\mathbf{A}}$  are the perturbed electrostatic and vector potentials. For a given Vlasov equilibrium and for a given choice of wave vector  $(k_x, k_y)$ , the code computes the real frequency, growth rate (real and imaginary part of  $\omega$ ), and the complex eigenfunctions  $\tilde{\phi}(z)$  and  $\tilde{\mathbf{A}}(z)$  which describe the mode structure. The resulting electric and magnetic field perturbations are computed from

$$\hat{\mathbf{E}} = -\nabla \hat{\phi} - \frac{1}{c} \frac{\partial \hat{\mathbf{A}}}{\partial t}$$

$$\hat{\mathbf{B}} = \nabla \times \hat{\mathbf{A}}.$$

[13] The eigenvalue problem is solved with a finite element expansion of the eigenfunction. Typical solutions presented in this manuscript employ 256 finite elements across the sheet to represent the eigenfunction. To evaluate the orbit integral, each particle trajectory is followed for a

single period  $\tau_p$  using a time step  $\Delta t = \tau_p/40$ . The velocity space grid is  $1000 \times 40 \times 40$  with the finer resolution in the  $v_x$  direction to fully resolve the perturbed distribution function in the vicinity of the resonance. The results presented in this manuscript have been carefully checked for numerical convergence and sensitivity to these parameters.

#### 4. Results

[14] In this section, the linear properties of the tearing mode are examined as a function of the guide field. Before discussing these new results, it is worth reviewing the basic properties of the tearing mode as a function of the dimensionless parameters (6) which are held fixed in this study. The variation of the growth rate with the mass ratio  $m_i/m_e$ , sheet thickness  $\rho_i/L$ , and temperature ratio  $T_i/T_e$  have been studied in previous work for a Harris sheet [*Daughton*, 1999]. Both the growth rate and the wavelength of the fastest-growing mode are very weakly dependent on the mass ratio  $m_i/m_e$ . This allows fairly realistic kinetic simulations of tearing to be conducted at artificial values of  $m_i/m_e$  without significantly altering the linear properties of the instability. For thicker current layers (smaller  $\rho_i/L$ ) the growth rate is rapidly reduced and the fastest-growing mode shifts to slightly longer wavelength  $k_x L \approx 0.3$ , while for thinner sheets the growth rate is increased and the fastest-

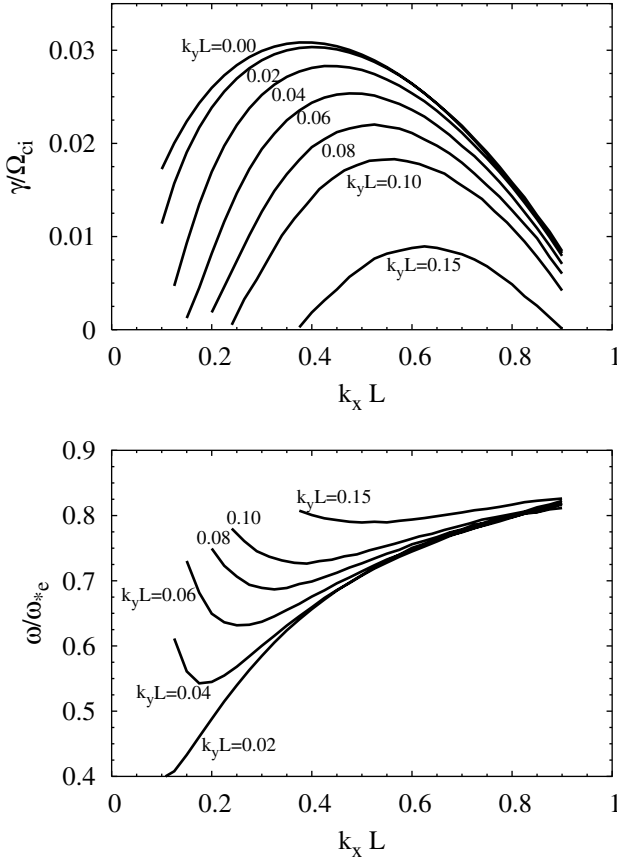


**Figure 3.** Dispersion relation in the limit of strong guide field  $B_{y0}/B_{x0} = 0.5$ . The (top) growth rate normalized to  $\Omega_{ci}$  and (bottom) real frequency normalized to  $\omega_{*e} \equiv k_y U_e$  are given as a function of  $k_x$  and  $k_y$  for the equilibrium parameters in (6).

growing mode is very near  $k_x L \approx 0.5$ . The growth rate is a fairly strong function of the electron temperature and is significantly reduced when the electron temperature is less than the ion temperature  $T_i/T_e > 1$ . The growth rate, real frequency, and electromagnetic contribution to the eigenfunction  $\mathbf{A}$  are to a very good approximation independent of the ratio  $\omega_{pe}/\Omega_{ce}$ . However, the magnitude of the electrostatic contribution to the eigenmode scales linearly with this dimensionless parameter. Therefore in this manuscript, the electrostatic contribution to the eigenfunction is presented in terms of the rescaled potential

$$\phi^*(z) \equiv \tilde{\phi}(z) \frac{\omega_{pe}}{\Omega_{ce}}. \quad (8)$$

Presented in this form, all aspects of the linear theory are independent of  $\omega_{pe}/\Omega_{ce}$ . This remains true for all values of the guide field. The only regime in which significant deviations are observed is for  $\omega_{pe} < \Omega_{ce}$ , which corresponds to relativistic electrons. Since the linear theory is based on the nonrelativistic Vlasov equation, this regime is not considered in the present manuscript.

[15] Although the tearing mode has been thoroughly examined in the limit of very strong guide field, the transitional regime between a neutral sheet with meandering

electron orbits and the strong guide field limit with helical electron orbits has not been carefully examined. As one might expect, the properties of the tearing mode are largely determined by the degree electron orbits are modified by the presence of the guide field. In a neutral sheet with  $B_y = 0$ , the electrons in the central region undergo meandering orbits with spatial extent  $\delta_e = \sqrt{2\rho_e L}$  where  $\rho_e = v_{th,e}/\Omega_{ce}$  is a thermal electron gyroradius computed with  $B_{x0}$ . In the opposite limit of strong guide field, the electrons are fully magnetized and undergo helical trajectories with weak guiding center drifts due to the field inhomogeneity. A rough estimate for the magnetic field required to magnetize the electrons in the central region is determined by setting  $\delta_e \approx \rho_{eG}$ , where  $\rho_{eG}$  is a thermal electron gyroradius in the guide field. This simple estimate results in a characteristic guide field

$$\frac{B_y^*}{B_{x0}} \equiv \frac{1}{\sqrt{2}} \left( \frac{\rho_i}{L} \right)^{1/2} \left( \frac{T_e m_e}{T_i m_i} \right)^{1/4}, \quad (9)$$

for which the trajectory of a thermal electron is significantly modified. In this manuscript, the regime  $B_{y0} < B_y^*$  is referred to as the weak guide field limit, since the electron trajectories are still primarily influenced by the Harris field  $B_x(x)$ . The opposite limit  $B_{y0} \gg B_y^*$  is referred to as the strong guide field regime, since the electrons are fully magnetized by the guide field. In addition, there is an intermediate range of guide fields corresponding to the transitional regime between the unmagnetized and fully magnetized electron trajectories. The simple estimate (9) corresponds roughly to the magnetic field required to magnetize an electron travelling at a thermal speed  $v_{th,e}$ . In order to strongly magnetize all the electrons in the distribution, a magnetic field 2–3 times larger than  $B_y^*$  is required. Therefore we adopt the following nomenclature to describe the strength of the guide field:

$$B_{y0} < B_y^* \rightarrow \text{Weak},$$

$$B_y^* < B_{y0} < 3B_y^* \rightarrow \text{Intermediate}, \quad (10)$$

$$B_{y0} > 3B_y^* \rightarrow \text{Strong}.$$

The numerical value of “3” in the above designation is of course somewhat arbitrary. However, as discussed in section 4.4, the behavior of the tearing mode growth rate as a function of the guide field does indeed break into three distinct regimes consistent with the designation in (10). In the following three subsections, the mode structure and dispersion relation are discussed for each of these regimes.

#### 4.1. Weak Guide Field

[16] The dispersion relation of the tearing mode in the limit of zero guide field is shown in Figure 1 for the parameters in (6). The fastest-growing mode occurs for approximately  $k_x L \approx 0.46$  and  $k_y L = 0$ . For parameter regimes in which tearing is less strongly driven (thicker sheet, colder electrons), the fastest-growing mode shifts to somewhat longer wavelength. Regardless of the other equilibrium parameters, in the limit of weak guide field the fastest-growing tearing mode always has  $k_y \rightarrow 0$ . As

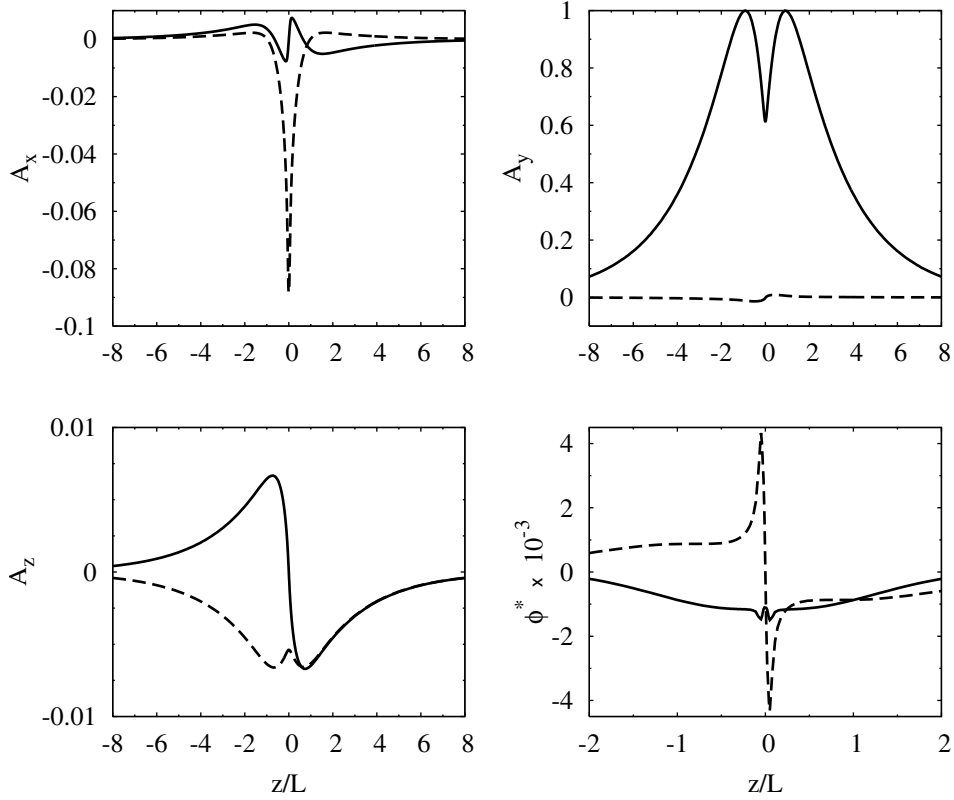


**Figure 4.** Example eigenfunction for a tearing mode with strong field  $B_{y0}/B_{x0} = 0.5$  and equilibrium parameters in (6). The solid and dashed lines denote the real and imaginary parts of  $A_x$ ,  $A_y$ ,  $A_z$  and  $\phi^* \equiv \tilde{\phi} (\omega_{pe}/\Omega_{ce})$ . The wave vector is  $k_x L = 0.40$ ,  $k_y L = 0$  and the growth rate is  $\gamma/\Omega_{ci} = 0.031$ . The range of  $z/L$  displayed in  $\phi^*$  figure is expanded to better show the rapid transition across the resonant surface at  $z/L = 0$ .

shown in Figure 1, the addition of finite  $k_y$  introduces a linear coupling to the drift mode which reduces the growth rate and causes the mode to propagate in the direction of electron drift  $U_e$  with frequency of order  $\omega_{e*} \equiv k_y U_e$ , the electron diamagnetic drift frequency. Therefore in this manuscript it is convenient to normalize the real frequency to  $\omega_{e*}$ , while retaining the more standard normalization for the growth rate in terms of the ion cyclotron frequency  $\Omega_{ci}$  based on the lobe field.

[17] A typical eigenfunction for the case of no guide field is shown in Figure 2. Although most theoretical treatments include only the  $A_y$  component of the perturbation, the tearing mode actually perturbs all three components of the vector potential as well as the electrostatic potential. Each component of the eigenfunction is of definite symmetry, with  $A_x$ ,  $A_y$  and  $\tilde{\phi}$  of even parity and  $A_z$  of odd parity. As discussed in section 4.7, the subdominant component of the electromagnetic perturbation gives rise to an out-of-plane magnetic field perturbation, which is an important signature of the collisionless tearing instability.

[18] The electrostatic contribution is important in accurately computing the growth rate for ion scale current sheets [Hoshino, 1987] but is less important for thicker current layers. The electrostatic contribution to the tearing eigen-

function in Figure 2 is rescaled by the dimensionless parameter  $\omega_{pe}/\Omega_{ce}$  as defined in (8). Presented in this fashion, the function  $\phi^*(z)$  is independent of  $\omega_{pe}/\Omega_{ce}$ . The relative importance of the electrostatic to electromagnetic perturbation may be estimated directly from Figure 2. In this manuscript, the normalizations employed for the tearing eigenfunction is the same as standard PIC units, where time is normalized to the electron plasma frequency  $\omega_{pe}$  and length is normalized to the electron skin depth  $c/\omega_{pe}$ . Thus to compare the electrostatic to electromagnetic contributions to the perturbed electric field  $\tilde{E}_x$ , one would compare  $(k_x c/\omega_{pe})\tilde{\phi}$  to  $(\omega/\omega_{pe})A_x$ . For the example in Figure 2, the wave vector is  $k_x c/\omega_{pe} \approx 0.017$  and  $|\omega|/\omega_{pe} \approx 8.2 \times 10^{-6}$ , which implies that  $\tilde{E}_x$  is dominated by the electrostatic contribution. Likewise,  $\tilde{E}_z$  is also dominated by the electrostatic contribution. Furthermore, it is easy to show this result is independent of the ratio  $\omega_{pe}/\Omega_{ce}$  for both  $\tilde{E}_x$  and  $\tilde{E}_z$ . With this in mind, the ratio of the magnetic field to electric field perturbation is  $\tilde{B}_z/\tilde{E}_x = \tilde{A}_y/\tilde{\phi}$ , which is directly proportional to  $\omega_{pe}/\Omega_{ce}$ . Thus the relative magnitude of the electrostatic perturbation is significantly reduced in the physically relevant parameter regime for magnetospheric plasmas  $\omega_{pe}/\Omega_{ce} \sim 8$ . This may have implications for the nonlinear saturation of the tearing mode even though the linear growth rate is independent of  $\omega_{pe}/\Omega_{ce}$ .

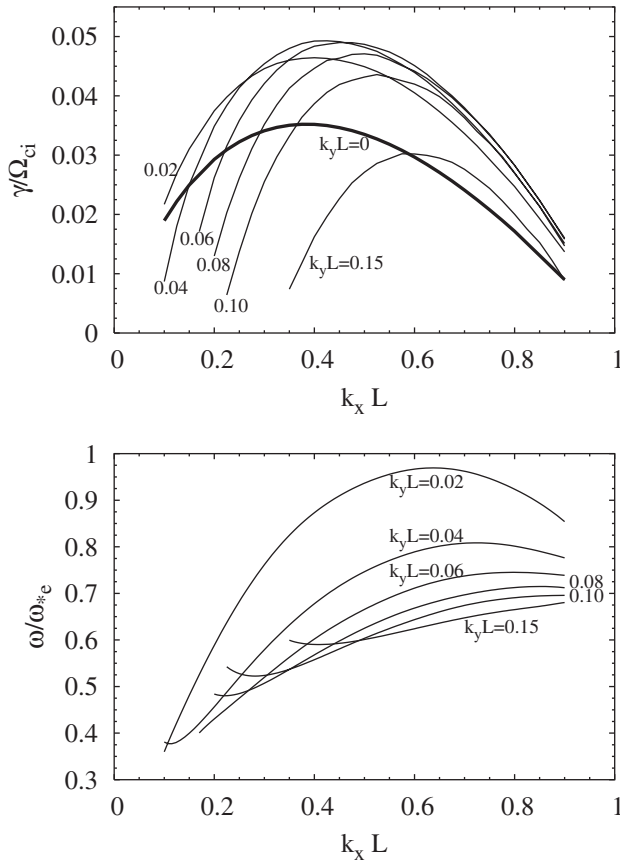


**Figure 5.** Dispersion relation in the limit of intermediate guide field  $B_{y0}/B_{x0} = 0.2$ . The (top) growth rate normalized to  $\Omega_{ci}$  and (bottom) real frequency normalized to  $\omega_{*e} \equiv k_y U_e$  are given as a function of  $k_x$  and  $k_y$  for the equilibrium parameters in (6).

#### 4.2. Strong Guide Field

[19] An example dispersion relation for the strong guide field regime is shown in Figure 3 for the equilibrium parameters in (6). The wave vector of the fastest-growing mode is approximately  $k_x L \approx 0.4$ . The addition of finite  $k_y$  reduces the growth rate as predicted by a large body of previous work on drift tearing modes for strong guide field [Catto *et al.*, 1974; Coppi *et al.*, 1979; Galeev, 1983; Kuznetsova and Zelenyi, 1985; Gladd, 1990]. With the addition of finite  $k_y$ , the phase velocity of the mode is in the direction of the electron drift with a real frequency of order  $\omega_{*e}$ . The resulting growth rate for the drift tearing mode is significant over a fairly broad range of angles extending to  $\theta \approx 15^\circ$ . This is a broader range than previous results reported by Gladd [1990] for drift tearing. However, this previous work considered much thicker current sheets  $\rho_i/L = 0.1$  and the approach involved a large number of approximations.

[20] A typical tearing eigenfunction for the limit of strong guide field is shown in Figure 4 for the fastest-growing mode in Figure 3. The symmetry properties are complicated by the presence of a guide field but are not destroyed entirely. Each component of the eigenfunction is a superposition of even and odd parity contributions which are  $90^\circ$

out of phase. Of course, one may decompose any arbitrary complex function into even and odd parity contributions; however, if the function lacked any symmetry properties, both parities would contain both real and imaginary parts. In contrast, for each component in Figure 4, both the real and imaginary parts are of definite parity.

[21] The dominant component of the tearing eigenfunction  $A_y$  is even parity and gives rise to the formation of the magnetic island. This part of the tearing mode structure is very similar to the case of zero guide field in Figure 2. In contrast, the structure of the mode arising from the three subdominant components of the eigenfunction is noticeably different than the zero guide field case. The relative magnitude of the electrostatic contribution is considerably larger and is dominated by an odd parity contribution which varies rapidly across the resonance layer and gives rise to a much stronger perturbation in  $\tilde{E}_z$ . The characteristic scale of this structure is a few  $\rho_{eG}$ . In addition, the subdominant electromagnetic perturbation  $\tilde{A}_x$  and  $\tilde{A}_z$  are composed of both odd and even parity terms. As discussed in section 4.7, this has important implications for the out-of-plane magnetic field perturbation.

#### 4.3. Intermediate Guide Field

[22] An example dispersion relation for an intermediate guide field is shown in Figure 5 for the parameters in (6). In contrast to either the weak or strong guide field regimes, the fastest-growing instability is an obliquely propagating drift tearing mode. For these parameters, the maximum growth rate  $\gamma/\Omega_{ci} \approx 0.05$  occurs approximately for  $k_x L \approx 0.45$ ,  $k_y L \approx 0.05$ , corresponding to an oblique angle of  $\theta = \tan^{-1}(k_y/k_x) \approx 6.3^\circ$ . This is nearly 40% faster than the conventional tearing mode with  $k_y = 0$ , which has a growth rate  $\gamma/\Omega_{ci} \approx 0.035$  for this example. For larger oblique angles  $k_y L > 0.05$ , the growth rate of the drift tearing mode is reduced and shifts to somewhat shorter wavelength. The growth rate of the drift tearing mode is approximately equal to the standard tearing mode near  $k_y L \approx 0.14$  corresponding to an oblique angle of  $\theta \approx 16^\circ$ .

[23] A typical eigenfunction for the tearing mode in the intermediate guide field regime is shown in Figure 6 for the wave vector  $k_x L = 0.40$  and  $k_y L = 0$ . The basic features are quite similar to the strong guide field case in Figure 4, although the relative amplitudes between the various components are a bit different. The symmetry properties for this case are identical to the preceding discussion for Figure 4.

[24] With the addition of finite  $k_y$ , the properties of the eigenfunction are dramatically altered. The tearing instability localizes about the resonant surfaces within the current sheet where  $\mathbf{k} \cdot \mathbf{B} = 0$ . For the equilibrium magnetic field in (1), the resonant surfaces are located at

$$\frac{z}{L} = -\tanh^{-1} \left( \frac{k_y B_{y0}}{k_x B_{x0}} \right) \approx -\frac{k_y B_{y0}}{k_x B_{x0}}, \quad (11)$$

where the approximate expression is the lowest-order expansion assuming  $k_y B_{y0} \ll k_x B_{x0}$ . For the drift tearing mode, the  $y$ -component of the wave vector is always in the direction of the electron drift  $U_e$  which is the negative  $y$ -direction. The  $x$ -component of the wave vector  $k_x$  may be either positive or negative. For the case of a neutral sheet

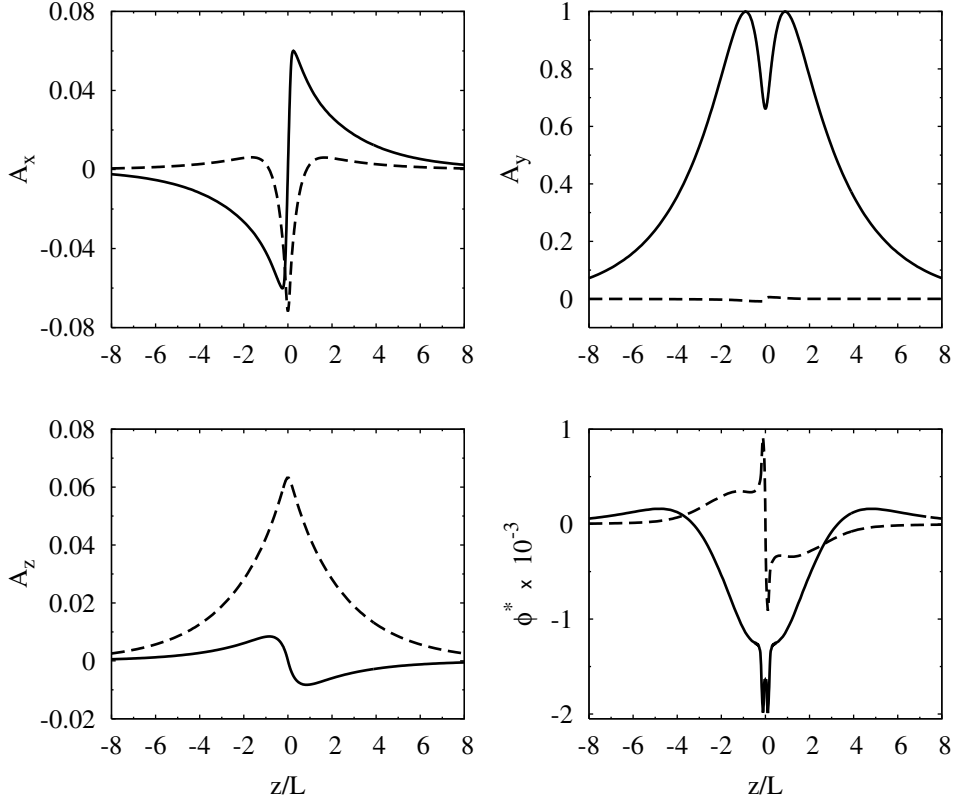


**Figure 6.** Example eigenfunction for a tearing mode at intermediate guide field  $B_{y0}/B_{x0} = 0.2$  with equilibrium parameters in (6). The solid and dashed lines denote the real and imaginary parts of  $A_x$ ,  $A_y$ ,  $A_z$  and  $\phi^* \equiv \phi(\omega_{pe}/\Omega_{ce})$ . The wave vector is  $k_x L = 0.40$ ,  $k_y L = 0$  and the growth rate is  $\gamma/\Omega_{ci} = 0.035$ .

$B_{y0} = 0$ , there is a single resonant surface at  $z = 0$  and consequently a single location for tearing to go unstable regardless of the magnitude of  $k_y$ . Since the mode remains localized at  $z = 0$ , the resulting eigenfunction retains clear symmetry properties. With the addition of a guide field, a finite  $k_y$  component destroys all symmetry in the problem. For a given wave vector, there are two resonant surfaces located on opposite sides of the current sheet and therefore two spatial locations where tearing modes can exist. The tearing mode with positive  $k_x$  is localized about the resonant surface on the  $z > 0$  side of the sheet, while the tearing mode with negative  $k_x$  is localized about the resonant surface on the  $z < 0$  side. Both the real frequency and growth rate for these two modes are exactly the same, but the localization, spatial mode structure, and direction of propagation are different. In the limit  $k_y \rightarrow 0$ , the resonant surfaces on each side of the sheet approach  $z \rightarrow 0$  and these two modes become one in the same. To emphasize this point, the eigenfunction for a drift tearing mode localized on the  $z > 0$  side of the layer is shown in Figure 7, while the eigenfunction for the corresponding mode localized on the  $z < 0$  side of the layer is shown in Figure 8.

#### 4.4. Maximum Growth Versus Guide Field

[25] The maximum growth rate of the tearing mode as a function of the guide field is shown in Figure 9 for the equilibrium parameters in (6). The solid line was computed by scanning over a range of  $k_x$  while holding  $k_y = 0$  in order

to locate the maximum growth rate for each value of the guide field. The dashed line was computed by scanning over both  $k_x$  and  $k_y$  in order to locate the maximum. The vertical lines correspond to  $B_y^*$  and  $3B_y^*$  so that one may easily infer the weak, intermediate, and strong guide field regimes based on the criteria in (10). As already discussed, the fastest-growing modes for both the weak and strong guide field occurs for  $k_y = 0$ , while the fastest-growing modes in the intermediate guide field regime occur at finite  $k_y$ .

[26] Note that changing the guide field from 0 to a value equal to the main field changes the growth rate by a factor of  $\sim 3.75$ . This indicates that component merging (finite guide field) at the magnetopause remains competitive to the antiparallel regime (zero guide field) for relatively large values of guide field. We will discuss this in more detail in Paper III.

[27] The physics responsible for the shift of the maximum growth to oblique angles in the intermediate regime is not well understood. We have verified that it is not due to the nonadiabatic contribution of ions, as the maximum growth remains oblique even when we turn off the nonadiabatic ion contribution in the linear code. So this shift has to do with the properties of electron orbits. The growth rate of the collisionless tearing instability is determined in part by the nature of the resonant interaction between the electrons and the mode. In the intermediate guide field regime, there exists a mixture of electron orbits, those that execute

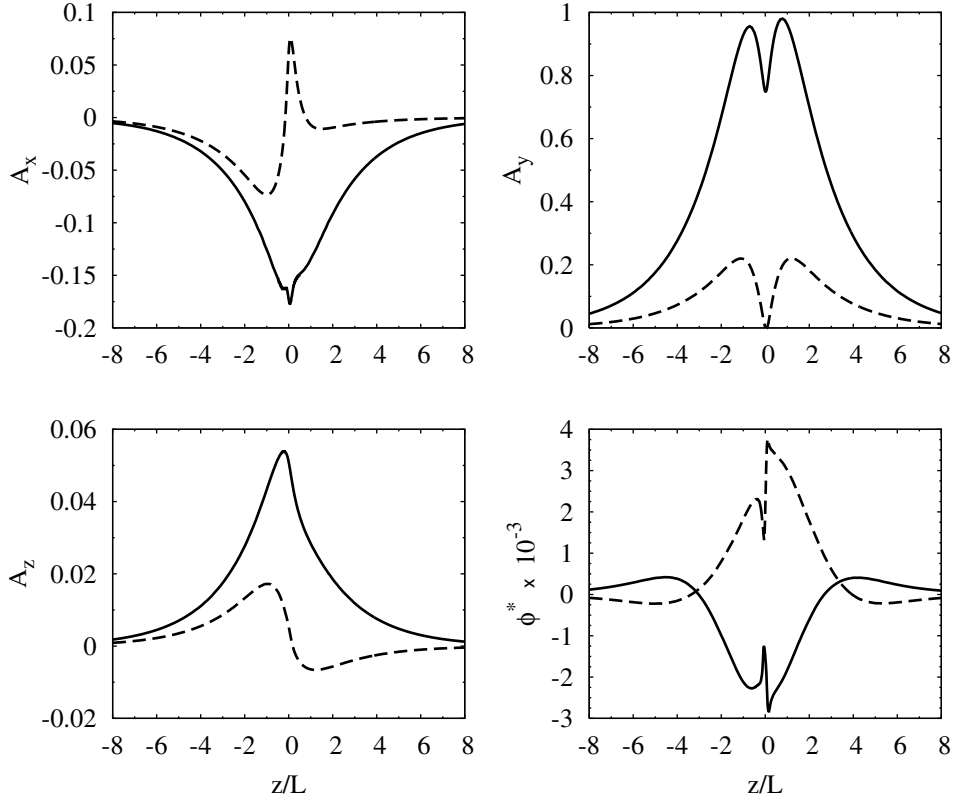


**Figure 7.** Example eigenfunction for a drift tearing mode at intermediate guide field  $B_{y0}/B_{x0} = 0.2$  with equilibrium parameters in (6). The solid and dashed lines denote the real and imaginary parts of  $\tilde{A}_x$ ,  $\tilde{A}_y$ ,  $\tilde{A}_z$  and  $\phi^* \equiv \tilde{\phi}(\omega_{pe}/\Omega_{ce})$ . The wave vector is  $\mathbf{k}L = (0.45\hat{x} - 0.06\hat{y})$ , the growth rate is  $\gamma/\Omega_{ci} \approx 0.049$  and the real frequency is  $\omega/\Omega_{ci} \approx 0.039$  which corresponds to  $\omega/\omega_{*e} \approx 0.82$ . The resonant surface where  $\mathbf{k} \cdot \mathbf{B} = 0$  is at  $z/L \approx 0.027$  for this mode.

complicated meandering orbits as in the zero guide field limit and those that are magnetized as in the strong guide field limit. This mixture of electron orbits leads to a mode that has properties intermediate between the two regimes of zero and strong guide field.

#### 4.5. Comparison With Analytic Theory

[28] One question of interest is the accuracy of previous approximate linear theories for collisionless tearing. Although there are analytic theories for both the neutral sheet and strong guide field limits, there does not appear to be any published analytic linear theory for the intermediate regime. In addition, previous analytic theories still involve a large number of approximations that become less accurate in the limit of a thin current layer. In Figure 9, the analytic growth rate is compared against the formally exact linear Vlasov code as a function of guide field and holding  $k_x L = 0.4$  fixed within the analytic calculation. The flat part of this curve in the weak guide field regime corresponds to the growth rate predicted by the analytic model for a neutral sheet (see equation (A24) in paper III), while the decreasing portion of the curve corresponds to the analytic result for a strong guide field (see equation (A23) in paper III). Thus the curve labelled “analytic model” in Figure 9 is the intersection of these two separate theories. In both cases, the analytic theory is larger than the prediction from the linear Vlasov

code, which is to be expected since the analytic theories neglect the contribution from resonant ions and furthermore neglect the electrostatic contribution to the mode. Presently, there is no analytic model that goes continuously through the intermediate regime. In the following two paragraphs, the analytic theories are compared for the weak and strong guide field limits as a function of the sheet thickness.

[29] Figure 10a shows a comparison for the growth rate predicted by analytic theory with the formally exact linear Vlasov code for the zero guide field limit. Since the effect of resonant ions are typically ignored in the analytic theory, we also show the result obtained from the linear Vlasov code with the resonant ion contribution removed (i.e., only include the adiabatic term for the ions). As explained in Paper III, one can derive two analytical theories, a simplified version that leads to a closed form solution (see equation (A24) in paper III) and a more complete treatment which requires a partial numerical solution (see equation (A27) in paper III). The simplified version does not predict the maximum  $k_x$ , whereas the more complete version predicts  $k_x L = 0.36$  as compared with 0.44 from the linear Vlasov code. In Figure 10a, we have used  $k_x L = 0.4$  to compute the growth rate curve for the analytical results. Other parameters in this comparison include  $T_i/T_e = 5$  and  $m_i/m_e = 1836$ . The simple analytical expression then yields  $\gamma \approx 0.0364(\rho_i/L)^{2.5}$  (dashed green line), whereas the semi-

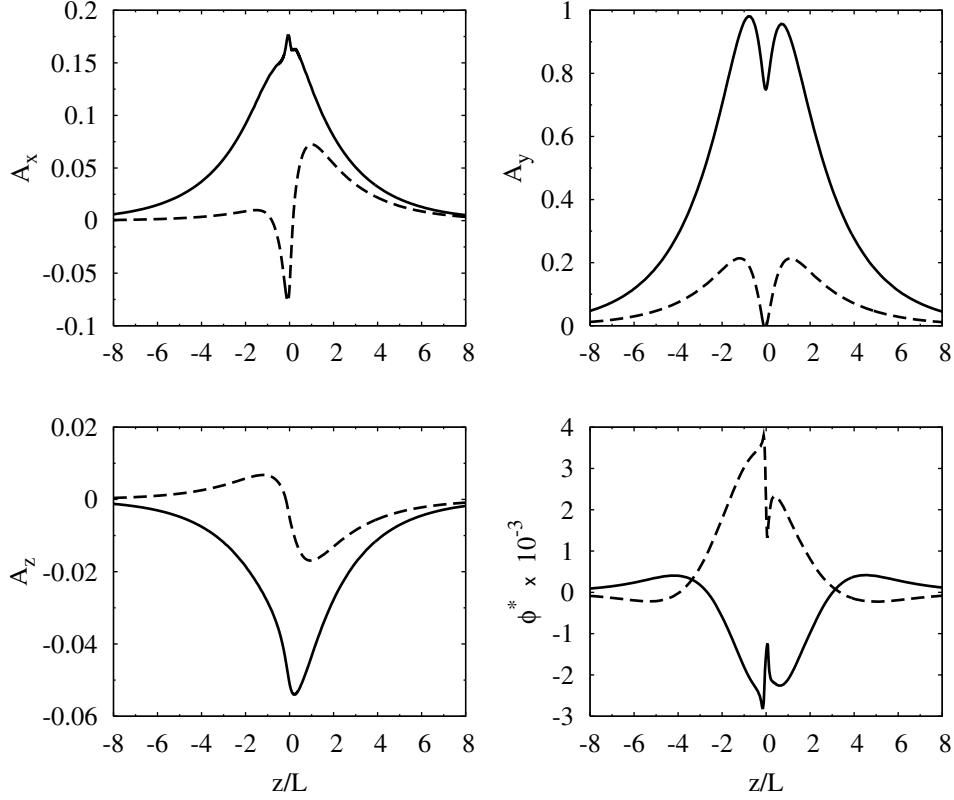


**Figure 8.** Example eigenfunction for a drift tearing mode at intermediate guide field  $B_{y0}/B_{x0} = 0.2$  with equilibrium parameters in (6). The solid and dashed lines denote the real and imaginary parts of  $\tilde{A}_x$ ,  $\tilde{A}_y$ ,  $\tilde{A}_z$  and  $\phi^* \equiv \tilde{\phi}(\omega_{pe}/\Omega_{ce})$ . The wave vector is  $\mathbf{k}L = (-0.45\hat{x} - 0.06\hat{y})$ , the growth rate is  $\gamma/\Omega_{ci} \approx 0.049$  and the real frequency is  $\omega/\Omega_{ci} \approx 0.039$  which corresponds to  $\omega/\omega_{*e} \approx 0.82$ . The resonant surface where  $\mathbf{k} \cdot \mathbf{B} = 0$  is at  $z/L \approx -0.027$  for this mode.

analytical result (dashed blue line) yields  $\gamma \approx 0.049(\rho_i/L)^{2.39}$  for  $\rho_i/L = 0.1 \rightarrow 1$ . These results are to be compared with  $\gamma \approx 0.0352(\rho_i/L)^{2.28}$  fit to the exact linear result (black line) and  $\gamma \approx 0.046(\rho_i/L)^{2.38}$  when the resonant ion terms are turned off in the linear code (red line). From this comparison, it is clear that the semianalytical result is in very good agreement with the formally exact linear Vlasov code when the resonant ion contribution is removed. Turning off the ion term leads to larger growth rates as expected with the ion contributions becoming larger for thinner sheets (a  $\sim 35\%$  effect). The semianalytical theory provides a good estimate of the growth rate in the absence of the resonant ion effects. Comparison of the simple analytical expression with the exact results (when ions are turned off) appears to become less accurate for thicker sheets. This is counterintuitive, as we would have expected the agreement with analytical theory to improve for thicker sheets. It is possible that for thicker sheets with  $\rho_i/L \ll 0.1$ , the analytical theory becomes a better approximation to the exact linear theory. However, with the existing Vlasov code, calculations become very difficult for these thick current layers, since one must resolve the singular thickness in physical space as well as the resonance in velocity space. Near marginal stability as the pole approaches the real axis, the direct numerical solution becomes extremely difficult. This regime is not interesting in

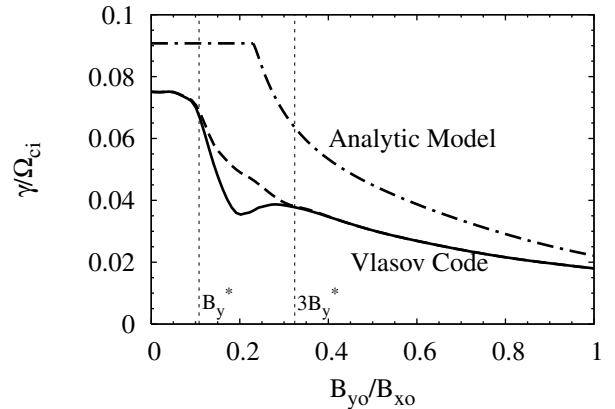


**Figure 9.** Maximum growth rate of tearing (solid) and drift tearing (dashed) as a function of guide field for realistic mass ratio  $m_i/m_e = 1836$  (see parameters in (6)). For the solid line,  $k_y = 0$  is held fixed and  $k_x$  is varied to find the maximum while for the dashed line both  $k_x$  and  $k_y$  are varied to find the maximum. In the weak and strong guide field regimes, the maximum growth occurs for  $k_y = 0$  while in the intermediate regimes maximum growth occurs for finite  $k_y$ . The analytic model for the growth rate (dashed-dot) was computed with  $k_x L = 0.4$ ,  $k_y = 0$  and is discussed in section 4.5.

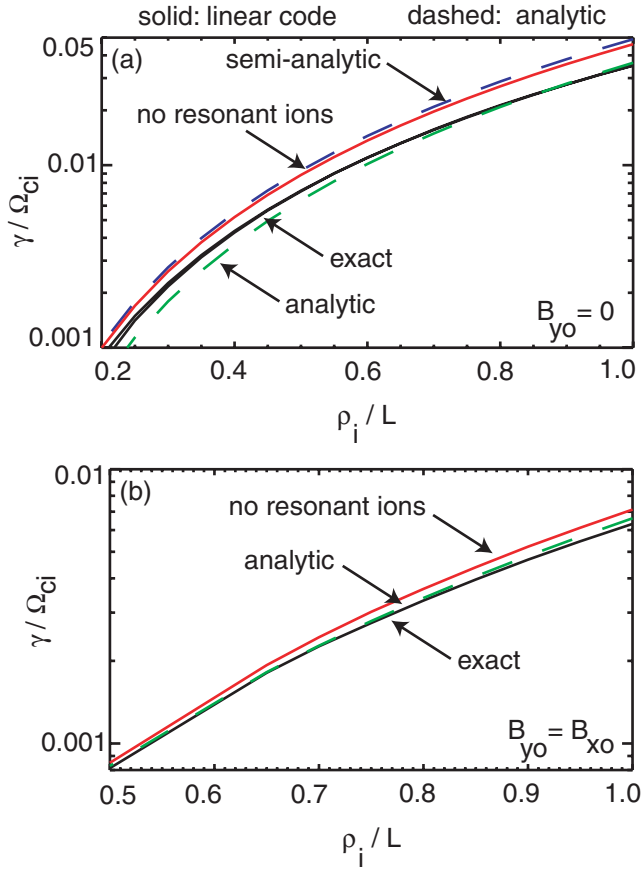


**Figure 10.** Comparison of maximum tearing mode growth rates as a function of sheet thickness  $\rho_i/L$  for (a) neutral sheet  $B_y = 0$  and (b) for strong guide field  $B_{y0} = B_{x0}$ . The solid black lines corresponds to the formally exact solution from the linear Vlasov code while the solid red lines were obtained by turning off the contribution from resonant ions within the calculation. The dashed green lines are from closed form analytic theory (see equation (A23)–(A24) in paper III), while the dashed blue line in the upper figure is a more complete semianalytic calculation (equation (A27) in paper III). Parameters in this comparison are  $m_i/m_e = 1836$  and  $T_i/T_e = 5$ .

magnetospheric physics, since the growth rates are far too small to be of significance.

[30] Next consider a comparison for the strong guide field limit shown in Figure 10b for  $B_{y0} = B_{x0}$ . In this case, the predicted growth rate from the full linear Vlasov calculation is well fit by  $\gamma \approx 0.00632 (\rho_i/L)^{2.9}$  (black line) and when the resonant ion contribution is removed this becomes  $\gamma \approx 0.00715 (\rho_i/L)^{3.0}$  (red line). The latter is in reasonable agreement with analytic theory (see equation (A23) in paper III), which for  $k_x L = 0.25$  yields  $\gamma \approx 0.00624 (\rho_i/L)^{3.0}$ . Thus the analytic theory provides a reasonable estimate of the growth rate, even for thin sheets. Turning off the ion term leads to larger growth rates but the effect is less pronounced than in the zero guide field case.

#### 4.6. Verification Using Kinetic Simulation

[31] The two-dimensional (2-D) kinetic simulation code is based on a well-known explicit electromagnetic algorithm

[Morse and Nielson, 1971; Forslund, 1985]. In this full-Maxwell approach, the fields are advanced using the scalar and vector potentials. Working in the Coulomb gauge, the scalar potential is computed directly from Poisson's equation, while the vector potential is advanced in time using a simple explicit algorithm [Morse and Nielson, 1971]. The particle trajectories are advanced using the leapfrog technique, and particle moments are accumulated with area weighting. To run on a parallel computer, the code is written using domain decomposition with calls to the MPI library. The boundary conditions for the particles and fields are periodic in the  $x$  direction. Conducting boundary conditions are imposed for the fields at the  $z$  boundaries, while reflecting boundary conditions are used for the particles.

[32] Even with the fastest available computers, it would be extremely difficult to simulate the development of a tearing mode for the equilibrium parameters in (6). Fortunately, the linear properties of tearing are only weakly dependent on the mass ratio  $m_i/m_e$  and the growth rate is completely independent of  $\omega_{pe}/\Omega_{ce}$ . Since the computational cost is a strongly increasing function of these two parameters, the simulations were performed with reduced values

$$\frac{\rho_i}{L} = 1, \quad \frac{m_i}{m_e} = 100, \quad \frac{T_i}{T_e} = 1, \quad \frac{\omega_{pe}}{\Omega_{ce}} = 3. \quad (12)$$

[33] For these simulation parameters, the maximum growth rate as function of guide field is shown in Figure 11. The solid line is the maximum growth rate with  $k_y = 0$ , while the dashed line was obtained by scanning over both  $k_y$  and  $k_x$ . The vertical lines correspond to  $B_y^*$  and  $3B_y^*$  for the simulation parameters in (12). The artificial mass ratio  $m_i/m_e = 100$  in Figure 11 results in approximately a 30% increase in the growth rate relative to the results at the physical mass ratio in Figure 9. As expected from (9), a larger  $B_y$  is required to transition

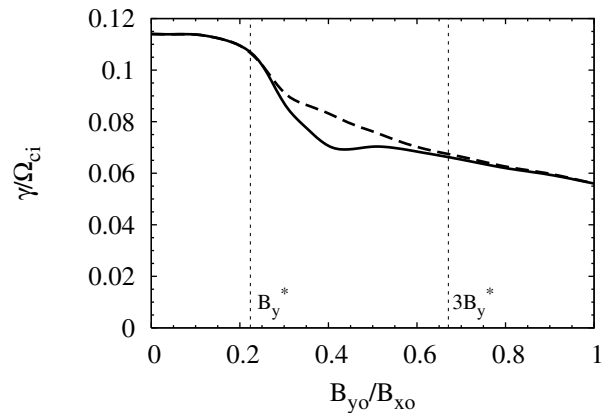


**Figure 11.** Maximum growth rate of tearing (solid) and drift tearing (dashed) as a function of guide field for the artificial mass ratio  $m_i/m_e = 100$  (parameters in (12)). For the solid line,  $k_y = 0$  is held fixed and  $k_x$  is varied to find the maximum while for the dashed line both  $k_x$  and  $k_y$  are varied to find the maximum. In the weak and strong guide field regimes, the maximum growth occurs for  $k_y = 0$  while in the intermediate regime maximum growth occurs for finite  $k_y$ .

**Table 1.** Comparison Between Kinetic Simulations and Linear Growth Rate Predictions in Figure 11

Case	$B_{y0}/B_{x0}$	$\theta$	$\gamma/\Omega_{ci}$ Theory	$\gamma/\Omega_{ci}$ Simulation
1	0.0	$0^\circ$	0.11	0.10
2	0.4	$0^\circ$	0.071	0.065
3	0.4	$5.7^\circ$	0.083	0.087
4	0.8	$0^\circ$	0.062	0.064

between the weak, intermediate, and strong guide field regimes. All of the basic features in Figure 11 are very similar to the physical mass ratio results in Figure 9. The largest difference in growth rate occurs for a guide field of  $B_{y0}/B_{x0} \approx 0.4$ . The tearing mode with  $k_x L = 0.5$  and  $k_y = 0$  has a predicted rate of  $\gamma/\Omega_{ci} \approx 0.071$ , while the drift tearing mode with  $k_x L = 0.50$  and  $k_y L = 0.05$  has a predicted growth rate  $\gamma/\Omega_{ci} \approx 0.083$ .

[34] There is an advantage in using 2-D simulations to verify the new linear predictions, since the simulation plane may be reoriented to permit or exclude the development of any particular mode. By orienting the simulation in the  $z$ - $x$  plane, only the standard tearing mode with  $k_y = 0$  is permitted to grow. Reorienting the simulation at an angle  $\theta = \tan^{-1}(k_y/k_x)$  relative to the  $z$ - $x$  plane will permit drift tearing modes with finite  $k_y$ , but will exclude the standard  $k_y = 0$  mode. Of course in reality all of these modes are unstable and will grow up simultaneously in a 3-D simulation. However, the limited goal of these 2-D simulations is to verify the new linear Vlasov predictions, and for this purpose it is desirable to exclude nonlinear interactions between the various unstable modes. The 2-D nonlinear evolution of tearing is considered extensively in Papers II and III.

[35] In order to verify the essential predictions in Figure 11, four simulations were performed over a range of guide fields. As shown in Table 1, one simulation is in the weak regime (case 1), one is in the strong regime (case 4), and two simulations are in the intermediate regime (case 2 and 3). In each case, the box size was  $4\pi L \times 4\pi L$ , which permits a single tearing island near maximum growth  $k_x L = 0.5$ . The spatial grid was  $512 \times 512$  spatial grid and  $30 \times 10^6$  computational particles were employed for each species. The time step was  $\Delta t \Omega_{ce} = 0.04$ . The linear growth rates shown in Table 1 were computed from a least squares regression over the linear phase. These simulation results confirm the predicted scaling of collisionless tearing as a function of the guide field and confirm drift tearing modes have a larger growth rate in the intermediate guide field regime.

#### 4.7. Out-of-Plane Magnetic Perturbation

[36] In the linear phase of collisionless tearing, the eigenfunction contains important information on the structure of the out-of-plane perturbation. The subdominant components of the eigenfunction ( $\tilde{A}_x$  and  $\tilde{A}_z$ ) give rise to the out-of-plane magnetic field perturbation  $\tilde{B}_y$ . In the limit of weak guide field, the perturbation has a quadrupole structure, as predicted from Hall MHD [Sonnerup, 1979]. In recent years, this quadrupole structure has been identified as a key signature of the Hall effect in fully nonlinear fast reconnection. Terasawa [1983] examined the properties of the out-of-plane magnetic perturbation for a neutral sheet with a linear eigenmode analysis of resistive Hall MHD.

The out-of-plane magnetic perturbation is also predicted by linear Vlasov theory, but as we now demonstrate, the characteristic structure is significantly different than in Hall MHD.

[37] The eigenfunctions resulting from linear Vlasov theory are used to examine how the structure of the out-of-plane perturbation varies as a function of the equilibrium guide field. In the limit of equal mass, the quadrupole structure disappears. Given this dependency on the mass ratio, we consider two cases, one with  $m_i/m_e = 100$  (Figure 12) and the other with  $m_i/m_e = 1836$  (Figure 13). On the left-hand side of each figure, the magnetic perturbation  $\tilde{B}_y$  computed from the eigenfunctions is shown for three different values of the guide field, corresponding to the limit of weak (Figure 2), intermediate (Figure 6), and strong guide field (Figure 4). In order to better visualize the predicted spatial structure, these solutions for  $\tilde{B}_y$  are used to construct the contour plots shown on the right-hand sides of Figures 12–13. Linear theory does not provide a prediction of the amplitude of the perturbation relative to the background field and only relative amplitudes and phases are physically meaningful. However, since in both observations and simulations of reconnection, it is the total  $B_y$  that is usually plotted, we show in Figures 12–13 contours of  $B_y(x, z) = \xi \text{Real}[\tilde{B}_y(x, z)] + B_{y0}$ . Here  $\xi$  is the amplitude of the linear perturbation relative to the background field. Linear theory does not provide an estimate for  $\xi$  nor does it take into account nonlinear addition of the imposed guide field on the underlying structure of  $\tilde{B}_y$ , which may become important in the nonlinear regime [Karimabadi et al., 1999]. Note that the choice of  $\xi$  only affects the values of the contours (i.e., the range of contour levels in the color bar) not the shape of the contours. However, it is still constructive to plot  $B_y$ , as it provides insight as to what the structure of the out-of-plane magnetic field would look like beyond the linear phase. Here we assume that the linear perturbation has grown to 60% of the background field.

[38] For the case of zero guide field, the real part of  $\tilde{B}_y$  is zero while the odd parity imaginary part gives rise to a quadrupolar structure. However, with the addition of a finite guide field the  $\tilde{B}_y$  perturbation is composed of both odd and even parity contributions, resulting in a distortion to the quadrupole structure. This distortion is most dramatic in the intermediate guide field regime (see middle panel), where the even parity contribution to  $\tilde{B}_y$  is larger than the odd parity term. For strong guide field, the odd parity term is again dominant and the spatial structure is compressed toward the electron scales. Thus the presence of the guide field both distorts and compresses the magnetic perturbation  $\tilde{B}_y$ . Another interesting point is that in both the intermediate and strong guide field limit in Figure 12,  $B_y$  has become positive everywhere. This is clearly a function of how large the linear perturbation grows relative to the initial guide field [Karimabadi et al., 1999].

[39] Next consider the out-of-plane magnetic perturbation at realistic mass ratio  $m_i/m_e = 1836$  in Figure 13. Comparing Figure 12 with Figure 13, several points are immediately obvious: (1) The extent of the core field in  $z$  is reduced significantly for realistic mass ratio in all cases, but the peak values of  $\tilde{B}_y$  remain almost the same. (2) The structure of  $\tilde{B}_y$  (or equivalently  $B_y$ ) is considerably different at realistic mass ratio, as the double peaked (blue) structure in the

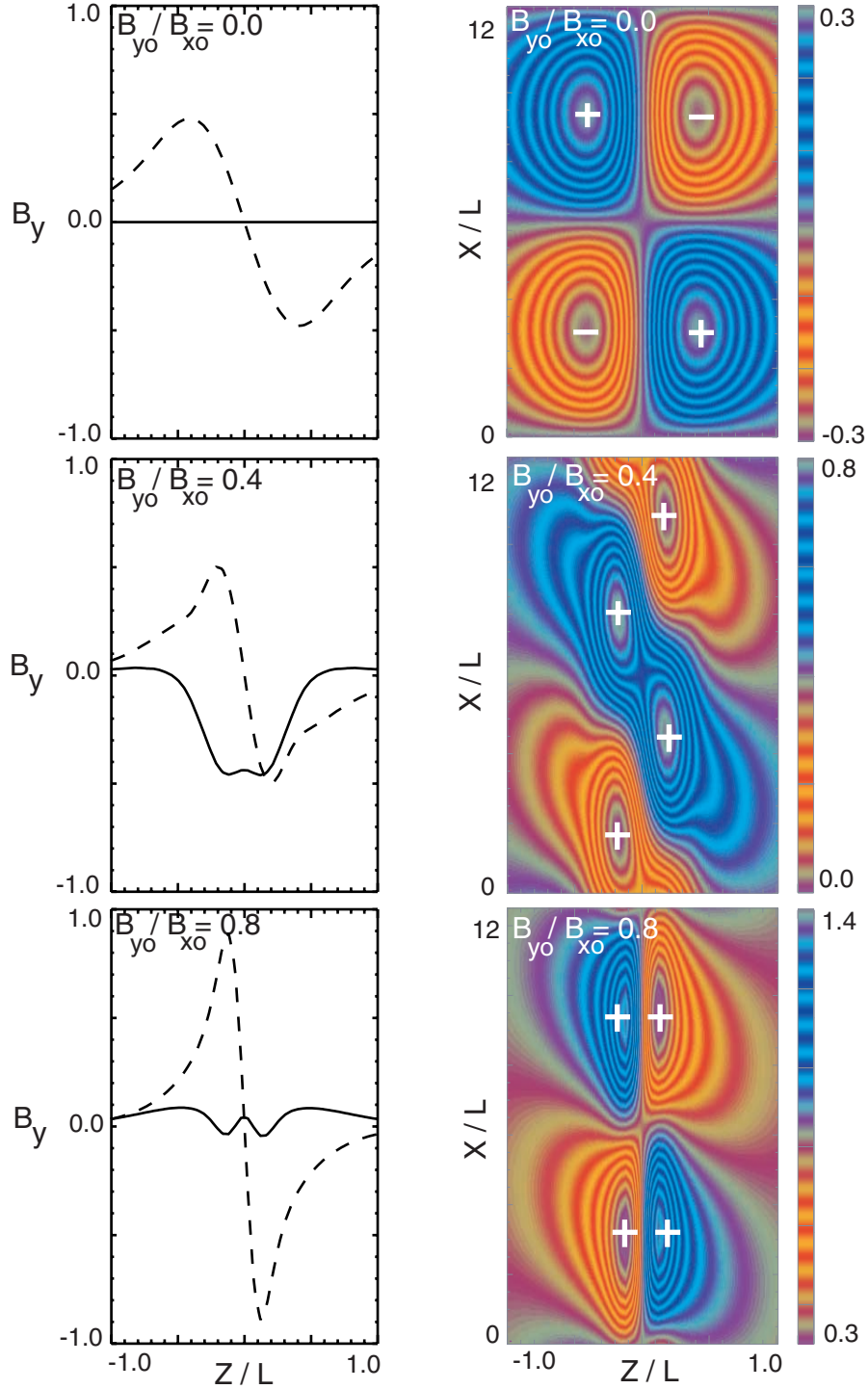


**Figure 12.** Linear Vlasov prediction for the out-of-plane magnetic field perturbation in the limit of (top) weak, (center) intermediate, and (bottom) strong guide field for mass ratio of 100. On the left-hand side, the solid and dashed lines denote the real and imaginary part of  $\tilde{B}_y(z)$  resulting from nonlocal linear Vlasov theory. On the right-hand side, the resulting contours of  $B_y(x, z) = B_{y0} + \xi(\cos(k_x x)\text{Real}[\tilde{B}_y(z)] - \sin(k_x x)\text{Imag}[\tilde{B}_y(z)])$  are used to visualize the predicted linear structure (where  $\xi = 0.6$ ). The equilibrium parameters are given in (6).

intensity plot of  $B_y$  has been replaced by a single peak in the central region.

[40] In the published literature, there are two physical mechanisms that contribute to the generation of the quadrupole structure. One is due to the Hall effect arising from

the difference in the electron and ion velocities [Sonnerup, 1979; Terasawa, 1983] and the other is due to ion kinetics [Karimabadi *et al.*, 2004]. The latter effect leads to quadrupole structures that can extend several ion inertial lengths, whereas Hall MHD produces thinner structures typically on

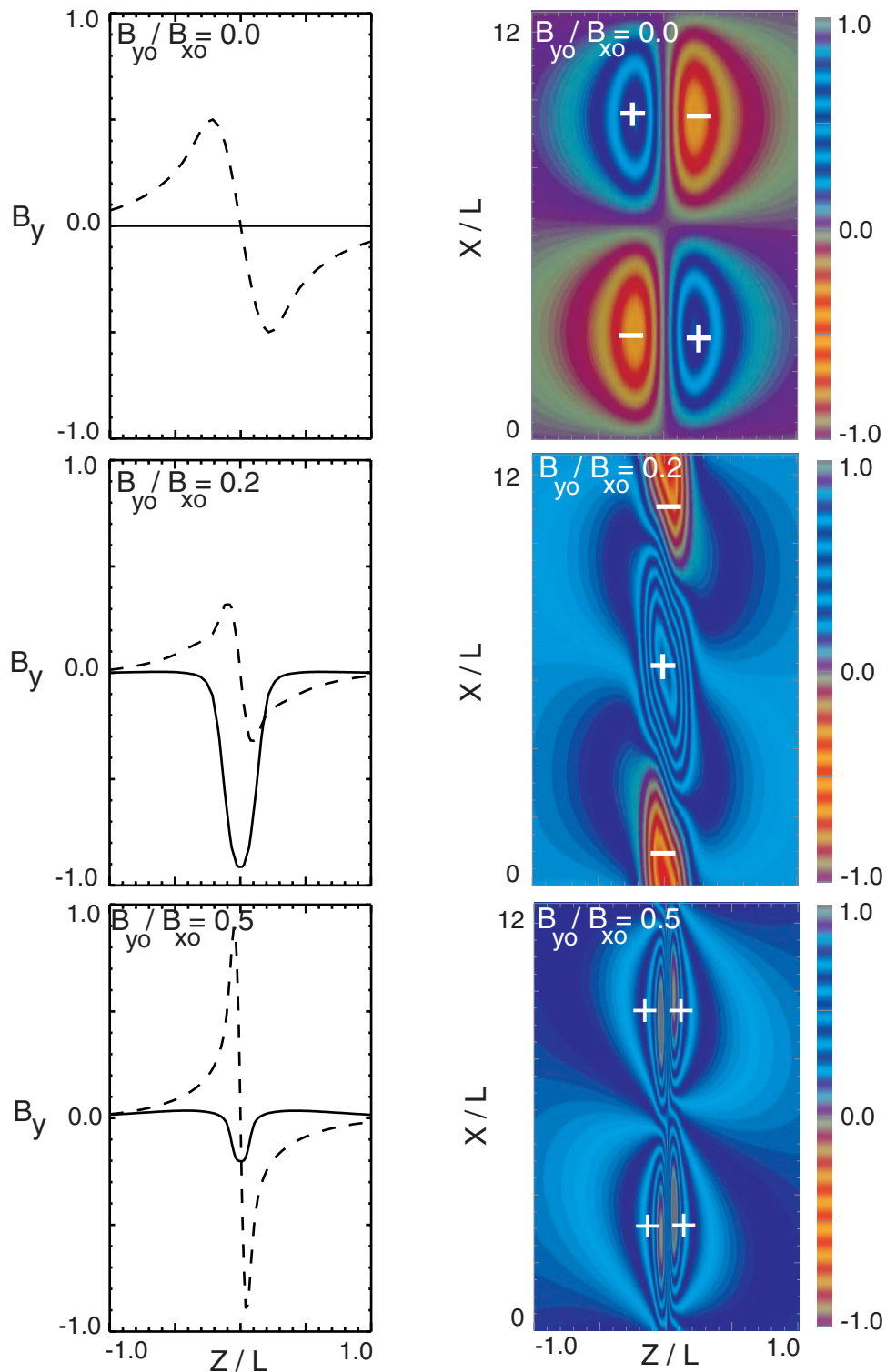


**Figure 13.** Same as Figure 12 except for realistic mass ratio  $m_i/m_e = 1836$  with equilibrium parameters in (6).

the order of ion inertial length. It is important to emphasize that the out-of-plane structures resulting from nonlocal linear Vlasov theory in Figure 13 are significantly smaller than the ion inertial length. For the neutral sheet limit, the spatial extent of the first peak in  $\tilde{B}_y$  is comparable to the scale  $\delta_e \approx 0.22L$  for crossing electron trajectories.

[41] It is instructive to compare these results with the prediction of resistive Hall MHD. In the Hall MHD eigenmode analysis [Terasawa, 1983] there are three relevant scales within the layer: an outer region where ideal MHD holds, an intermediate ion-inertial scale region where the Hall term becomes important, and finally the inner resonant

layer determined by the resistivity imposed within the calculation. When comparing against the eigenmode results from nonlocal Vlasov theory, one would expect the first two regions to be similar, but the scale of the resonant layer is determined by the electron kinetic physics instead of resistivity. In the Hall MHD results [Terasawa, 1983], the relative magnitude of the out-of-plane component of the perturbation  $\tilde{B}_y/\tilde{B}_x$  is predicted to be of order  $c/(\omega_{pe}L) \approx 1.4$ . In contrast, the Vlasov theory predicts a somewhat smaller ratio  $\tilde{B}_y/\tilde{B}_x \approx 0.6$  (not shown). In the Hall MHD theory, the peak in  $\tilde{B}_y$  is near the thickness of the resistive layer followed by a slower decrease extending outward to the ion inertial length. However, in the linear Vlasov treatment for a neutral sheet, the location of the peak value in  $\tilde{B}_y$  is set by the size of the electron meandering orbit followed by a slowly decreasing structure which can extend out to the ion inertial scale. Although the Hall effect plays an important role in the generation of the quadrupole structure, Hall MHD does not provide an adequate description of the out-of-plane structure, since it cannot properly describe the inner layer for a collisionless plasma.

[42] Although Terasawa [1983] did not consider the effect of a guide field, it is clear that Hall MHD cannot accurately describe the resonant layer in this regime either. For example, the intermediate regime identified in this manuscript is purely the result of electron kinetic effects and does not exist in Hall MHD or any plasma model with fluid electrons. Furthermore, in the strong guide field regime shown in Figure 13, the spatial extent of the first peak in  $\tilde{B}_y$  is reduced to approximately the electron gyro-radius in the guide field  $\rho_{eG} \approx 0.047L$ , indicating large finite electron gyroradius effects even in the presence of a strong guide field. Given this scaling, it would appear that reduced kinetic descriptions such as the gyrokinetic approach cannot fully describe this aspect of collisionless tearing even in the limit of very large guide field.

[43] For a collisionless tearing mode in the linear regime, both the characteristic form and spatial scale of the out-of-plane magnetic field perturbation are significantly different than predicted by previous researchers for fully developed fast reconnection. As reconnection proceeds to large amplitude, the spatial scale of these linear perturbations will be broadened due to (1) ion motion and (2) the expansion of the fields lines as one moves in a cone away from the x-point. Thus the linear theory provides the minimum scale length of the out-of-plane magnetic field in the vicinity of the x-line during the onset phase. These linear structures are quite difficult to compute with particle-in-cell kinetic simulations due to large statistical noise, and furthermore the linear regime is often bypassed by employing a large initial perturbation. However, in the magnetosphere these structures may perhaps provide an observable signature of collisionless tearing during the onset phase which is distinctly different than the much larger-scale out-of-plane structures observed during fast reconnection.

## 5. Conclusions

[44] The nonlocal kinetic theory of the collisionless tearing mode was reexamined as a function of guide field strength using a formally exact linear Vlasov code. Three distinct parameter regimes were identified as

function of the guide field. In the limit of weak guide field  $B_y < B_y^*$ , the electron trajectories are similar to a neutral sheet and the growth rate and properties of the eigenfunction are nearly independent of the guide field. For strong guide field  $B_y > 3B_y^*$ , the growth rate of tearing falls off approximately as  $B_{y0}^{-2/3}$ . For both the strong and weak guide field limits, the fastest-growing tearing modes have zero real frequency and are perpendicular to the current ( $k_y = 0$ ). However, in the intermediate guide field regime  $B_y^* < B_y < 3B_y^*$ , the fastest-growing tearing modes have a finite component of the wave vector in the direction of the current. These drift tearing modes propagate in the direction of the electron drift with real frequency comparable to the electron drift frequency. For a given  $k_y$  in the direction of the electron drift, there are two unstable drift tearing modes corresponding to  $\pm k_x$ , which are localized about resonant surfaces on opposite sides of the sheet. Thus to include the full spectrum of unstable drift tearing modes will require 3-D simulations. Nevertheless, the basic predictions from the linear Vlasov theory have been verified with 2-D fully kinetic simulations.

[45] The out-of-plane magnetic field perturbation predicted by linear Vlasov theory was examined in these three distinct regimes. In the limit of a neutral sheet, the familiar quadrupole structure is predicted, but the width and the relative amplitude are different than the Hall MHD prediction. The spatial scale of the peak value of  $\tilde{B}_y$  is of order  $\delta_e$  corresponding to a crossing electron orbit. Finite ion Larmor radius effects can lead to further broadening of the out-of-plane magnetic field perturbation in later stages of reconnection, leading to quadrupole structures extending over several ion inertial lengths [Karimabadi et al., 2004]. The addition of a guide field complicates the out-of-plane perturbation and compresses the spatial width down to the electron gyroscale. One question that is left for future work is the extent in which the structures predicted in linear theory may survive into the nonlinear regime. However, two features predicted by linear theory, namely the quadrupole structure in the zero guide field limit and the asymmetric structure for strong guide field, remain intact in the nonlinear stage, although the scale of the structures are typically larger than predicted by linear theory. Thus it may well be that the morphology of  $B_y$  as predicted by linear theory is preserved in the nonlinear regime, and as such linear theory would provide the minimum length scale for  $B_y$ . The fact that the scale length of  $B_y$  in the nonlinear regime would be larger than the linear theory prediction is not surprising, since linear theory does not take into account the cone angle of the reconnection layer around a x-point which leads to broadening of  $B_y$  away from the x-point, nor does it include ion scale effects [Karimabadi et al., 2004]. Finally, the growth rate of the tearing mode is not a strong function of the guide field, changing by a factor of  $\sim 3.75$  when the guide field changes from 0 to 1. The relevance of this finding and its implication for onset of reconnection at the magnetopause will be explored in detail in Paper III.

[46] **Acknowledgments.** The research of W. Daughton was supported by the Los Alamos National Laboratory Directed Research and Development program (LDRD), the NASA Geospace Science program, and an IGPP grant. The research of H. Karimabadi was supported by NASA SEC

Theory Program NAG5-11754, NSF grant ATM-9901665, and an IGPP grant. Authors acknowledge useful conversation with K. B. Quest.

[47] Shadia Rifai Habbal thanks two referees for their assistance in evaluating this paper.

## References

- Baumjohann, W., and G. Paschmann (1987), Solar wind-magnetosphere coupling: Processes and observations, *Phys. Scr. T*, 18, 61.
- Biskamp, D., and K. Schindler (1971), Instability of two dimensional collisionless plasmas with neutral points, *Plasma Phys.*, 13, 1013.
- Burkhardt, G. R., and J. Chen (1989), Collisionless tearing instability of a bi-maxwellian neutral sheet: An integrodifferential treatment with exact particle orbits, *Phys. Fluids B*, 8, 1578.
- Catto, P., A. E. Nadi, C. Liu, and M. Rosenbluth (1974), Stability of a finite- $\beta$  inhomogeneous plasma in a sheared magnetic field, *Nucl. Fusion*, 14, 405.
- Chen, J., and P. Palmadesso (1984), Tearing instability properties of an anisotropic neutral sheet, *Phys. Fluids*, 27, 1198.
- Coppi, B., G. Laval, and R. Pellat (1966), Dynamics of the geomagnetic tail, *Phys. Rev. Lett.*, 16, 1207.
- Coppi, B., J.-K. Mark, and L. Sugiyama (1979), Reconnecting modes in collisionless plasmas, *Phys. Rev. Lett.*, 42, 1058.
- Coroniti, F., and K. Quest (1984), Nonlinear evolution of magnetopause tearing modes, *J. Geophys. Res.*, 89, 137.
- Crooker, N. (1979), Dayside merging and cusp geometry, *J. Geophys. Res.*, 84, 951.
- Daughton, W. (1999), The unstable eigenmodes of a neutral sheet, *Phys. Plasmas*, 6, 1329.
- Daughton, W. (2003), Electromagnetic properties of the lower-hybrid drift instability in a thin current sheet, *Phys. Plasmas*, 10, 3103.
- Ding, D., L. Lee, and C. Kennel (1992), The beta-dependence of the collisionless tearing instability at the dayside magnetopause, *J. Geophys. Res.*, 97, 8257.
- Drake, J., and Y. Lee (1977), Kinetic theory of tearing instabilities, *Phys. Fluids*, 20, 1341.
- Forslund, D. (1985), Fundamentals of plasma simulation, in *Space Plasma Simulations*, edited by M. Ashour-Abdalla and D. Dutton, pp. 425–439, Springer, New York.
- Galeev, A. (1983), Plasma processes within the magnetosphere boundaries, *Space Sci. Rev.*, 34, 213.
- Galeev, A. A., and L. Zelenyi (1978), *Magnetic Reconnection in a Space Plasma*, 93 pp., Int. Atom. Energy Agency, Vienna.
- Galeev, A., M. Kuznetsova, and L. Zelenyi (1986), Magnetopause stability threshold for patchy reconnection, *Space Sci. Rev.*, 44, 1.
- Gladd, N. (1990), Collisionless drift-tearing modes in the magnetopause, *J. Geophys. Res.*, 95, 20,889.
- Gonzalez, W., and F. Mozer (1974), A quantitative model for the potential resulting from reconnection with an arbitrary interplanetary magnetic field, *J. Geophys. Res.*, 79, 4186.
- Gosling, J., M. Thomsen, S. Bame, and C. Russell (1990), Plasma flow reversals at the dayside magnetopause and the origin of asymmetric polar cap convection, *J. Geophys. Res.*, 95, 8073.
- Harris, E. G. (1962), On a plasma sheath separating regions of one directional magnetic field, *Nuovo Cimento*, 23, 115.
- Hesse, M., M. Kuznetsova, and M. Hoshino (2002), The structure of the dissipation region for component reconnection: Particle simulations, *Geophys. Res. Lett.*, 29(12), 1563, doi:10.1029/2001GL014714.
- Hoshino, M. (1987), The electrostatic effect for the collisionless tearing mode, *J. Geophys. Res.*, 92, 7368.
- Karimabadi, H., D. Krauss-Varban, N. Omid, and H. X. Vu (1999), Magnetic structure of the reconnection layer and core field generation in plasmoids, *J. Geophys. Res.*, 104, 12,313.
- Karimabadi, H., J. Huba, D. Krauss-Varban, and N. Omid (2004), On the generation and structure of the quadrupole magnetic field in the reconnection process: Comparative simulation study, *Geophys. Res. Lett.*, 31, L07806, doi:10.1029/2004GL019553.
- Karimabadi, H., W. Daughton, and K. Quest (2005a), Physics of saturation of collisionless tearing modes as a function of guide field, *J. Geophys. Res.*, A03214, doi:10.1029/2004JA010749.
- Karimabadi, H., W. Daughton, and K. Quest (2005b), Anti-parallel versus component merging at the magnetopause: Current bifurcation and intermittent reconnection, *J. Geophys. Res.*, A03213, doi:10.1029/2004JA010750.
- Kim, K.-H., N. Lin, C. A. Cattell, Y. Song, and D.-H. Lee (2002), Evidence for component merging near the subsolar magnetopause: Geotail observations, *Geophys. Res. Lett.*, 29(6), 1080, doi:10.1029/2001GL014636.
- Kuznetsova, M., and L. Zelenyi (1985), Stability and structure of the perturbations of the magnetic transitional layers, *Plasma Phys. Controlled Fusion*, 27, 363.
- Laval, G., R. Pellat, and M. Vuillemin (1966), Electromagnetic instabilities in a collisionless plasma, in *Plasma Physics and Controlled Nuclear Fusion*, vol. 2, p. 259, Int. Atom. Energy Agency, Vienna.
- Luhmann, J., R. Walker, C. Russell, N. Crooker, J. Spreiter, and S. Stahara (1984), Patterns of potential magnetic field merging sites on the dayside magnetopause, *J. Geophys. Res.*, 89, 1739.
- Moore, T., M. C. Fok, and M. Chandler (2002), The dayside reconnection x line, *J. Geophys. Res.*, 107(A10), 1332, doi:10.1029/2002JA009381.
- Morse, R., and C. Nielson (1971), Numerical simulation of the Weibel instability in one and two dimensions, *Phys. Fluids*, 14, 830.
- Newell, P., D. G. Sibeck, and C. I. Meng (1995), Penetration of the interplanetary magnetic field by and magnetosheath plasma into the magnetosphere: Implications for the predominant magnetopause merging site, *J. Geophys. Res.*, 100, 235.
- Quest, K. B., and F. Coroniti (1981a), Linear theory of tearing in a high- $\beta$  plasma, *J. Geophys. Res.*, 86, 3299.
- Quest, K. B., and F. Coroniti (1981b), Tearing at the dayside magnetopause, *J. Geophys. Res.*, 86, 3289.
- Sonnerup, B. (1974), Magnetopause reconnection rate, *J. Geophys. Res.*, 79, 1546.
- Sonnerup, B. (1979), Magnetic field reconnection, in *Solar System Plasma Physics*, edited by L. J. Lanzerotti, C. F. Kennel, and E. N. Parker, p. 46, Elsevier, New York.
- Sonnerup, B., H. Hasegawa, and G. Paschmann (2004), Anatomy of a flux transfer, *Geophys. Res. Lett.*, 31, L11803, doi:10.1029/2004GL020134.
- Terasawa, T. (1983), Hall current effect on tearing mode stability, *Geophys. Res. Lett.*, 10, 475.

W. Daughton, University of Iowa, Department of Physics and Astronomy, Iowa City, IA 52242, USA. (william-daughton@uiowa.edu)

H. Karimabadi, Department of Electrical and Computer Engineering, University of California, San Diego, 9500 Gilman Drive, La Jolla, CA 92093-0407, USA. (homa@ece.ucsd.edu)